Supporting Information

Compositing redox-rich Co-Co@Ni-Fe PBA nanocubes into cauliflower-like conducting polypyrrole as electrode material in supercapacitors

Poulami Mukherjee‡, Vishwanath R. S‡, Arie Borenstein, and Tomer Zidki**

Department of Chemical Sciences and the Centers for Radical Reactions and Materials Research, Ariel University, Ariel, 4077625 Israel.

Material Characterization. The crystal structures were evaluated by X-ray diffraction (XRD) patterns, recorded in the 2θ range of 10-80º (step size 0.02º and 5.0 s per step time) by Panalytical X'Pert Pro X-ray powder diffractometer with Cu Kα radiation,λ = 0.154 nm. The High-resolution scanning electron microscopy (HR-SEM) images were obtained by a Tescan MAIA3 equipped with an energy dispersive spectrometer (EDS) detector. Transmission electron microscopy (TEM) samples were prepared by dispersing the catalysts in a solution mixture of 2-propanol-water (1:1) and drop-casting them on carbon film-coated 300 mesh Cu grids. The TEM samples were allowed to dry overnight at room temperature for further analysis. Electron microscopy images were acquired using a Tecnai 12 microscopy (FEI) TEM and a JEM 2100, JEOL (200 kV) High-resolution TEM (HR-TEM). Fourier transform infrared (FTIR) spectra were obtained using Bruker Alpha II infrared spectrometer in a scan range of 4000-500 cm^{-1} in the TR mode. Thermogravimetric (TG) measurement was conducted in nitrogen at a temperature of 25-800°C with a heating rate of 10°C min^{-1} using a TA Q500 apparatus. The XPS samples were measured by an (XPS/AES) ESCALAB 250 Thermo Fischer Scientific instrument. The inductively coupled plasma plasma-optical emission spectroscopy (ICP-OES) analysis was performed using Spectro Acros optical emission spectrometer to determine the composition and the metal content in the samples.

Electrochemical measurements. The electrochemical measurements were performed in standard three-electrode systems using Biologic SP-150 potentiostat with 1.0 M Na_2SO_4 as electrolyte at room temperature. Graphite rod and Ag/AgCl were used as counter and reference electrodes. Cyclic voltammetry

(CV) experiments were performed at different scan rates with an applied potential range of -0.4 to 1.0 V. The galvanostatic charge-discharge (GCD) experiments were done in the potential range window of -0.4 to 0.8 V at different current densities (1 to 8 A g^{-1}). The average specific capacitance (C_s, F g^{-1}) values were calculated from CVs and GCD curves using **Eqs. S1** and **S2**. Furthermore, the specific capacity (Q_s, C g^{-1}) of Co-Co@Ni-Fe PBA-PPy and Co-Co@Ni-Fe PBA (showing battery-like behavior) was estimated using **Eq. S3**.

$$C_s = \frac{1}{mv\Delta V}\int i\,(V)dV \qquad \textbf{(S1)}$$

$$C_s = \frac{i \times \Delta t}{m \times \Delta V} \qquad \textbf{(S2)}$$

$$Q_s = \frac{i \times \Delta t}{m} \qquad \textbf{(S3)}$$

Where C_s is the specific capacitance (F g^{-1}), Q_s is the specific capacity (C g^{-1}), m signifies the mass of electrode materials, υ is the scan rate, i denotes the current (A), Δt represents the discharge time (s), and ΔV is a potential window (V). The area under the CV curve represents the current integration, which indicates the average current value. The electrochemical impedance spectroscopy (EIS) measurements were collected in the frequency range from 0.1 Hz to 100 kHz at the fully charged state with a perturbation amplitude of 5 mV.

An asymmetric supercapacitor (ASC) device was constructed using Co-Co@Ni-Fe PBA-PPy as the positive electrode, activated carbon (AC) as the negative electrode, and 1 M Na_2SO_4 as the electrolyte. AC was deposited on the carbon paper (CP) substrate using the working electrode's preparation method (section 2.4 in the manuscript). Both positive and negative electrodes were placed one upon another using a filter paper soaked in 1 M Na_2SO_4 as the separator, and all measurements were performed at room temperature. We determined the mass ratio of the positive (m_+) and negative (m_-) electrodes following the charge balance theory (**Eq. S4**). The C_s and Q_s values of the ASC device were calculated by their GCD curves using **Eq. S2** and **S3**, while the energy density (E, Wh kg^{-1}) and power density (P, W kg^{-1}) were calculated by **Eqs. S5** and **S6**.

$$\frac{m_+}{m_-} = \frac{C_{S-} \times \Delta V_-}{C_{S+} \times \Delta V_+} \quad \textbf{(S4)}$$

$$E = \frac{Q_S\,(\Delta V)}{7.2} \quad \textbf{(S5)}$$

$$P = E \times \frac{3600}{\Delta t} \quad \textbf{(S6)}$$

Where, $m_+, C_{S+}, \Delta V_+$ and $m_+, C_{S+}, \Delta V_+$ are the mass, specific capacitances, and potential windows of positive and negative electrode materials, respectively. The optimal mass ratio of the positive Co-Co@Ni-Fe PBA-PPy electrode to the negative AC electrode was determined to be about 0.75 (using **Eq S4**).

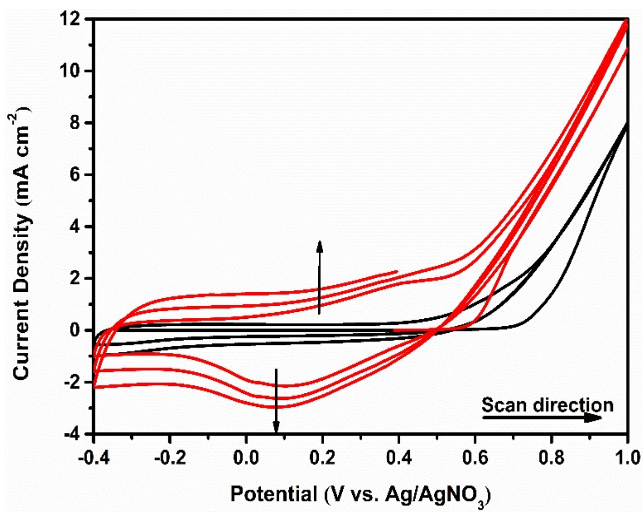

Fig S1. Electropolymerization deposition CVs (at 20 mV S^{-1}) of PPy on bare CP substrate (black) and Co-Co@Ni-Fe PBA coated CP substrate (Red) in acetonitrile containing 50 mM pyrrole and 0.1 M tetrabutylammonium hexafluorophosphate ($TBAPF_6$) supporting electrolyte.

As shown in **Fig S1**, subsequent CV cycles were performed to deposit PPy on the bare CP substrate (black) and Co-Co@Ni-Fe PBA-coated CP substrate (Red). Initially, the scan was started from open circuit potential and swept anodically up to 1.0 V vs. $Ag/AgNO_3$, during which the oxidative current increased as PPy deposition occurred. The oxidation potential of pyrrole was 0.75 V for bare CP substrate (black CVs) and 0.63 V for Co-Co@Ni-Fe core-shell PBA-coated CP substrate (red CVs). The polymerization started at a lower potential with core-shell PBA-coated CP substrate than bare CP. A pair of $Fe^{II/III}$ redox peaks developed along with PPy deposition in the subsequent cycles, signifying that even upon PPy deposition on Co-Co@Ni-Fe core-shell PBA, the redox behavior of the core-shell PBA complex retained because the nano-porous PPy provides constant ion transportation channels. Accordingly, the PPy deposition and doping of the Co-Co@Ni-Fe PBA-PPy composite with PF_6^- anions happened simultaneously. The mass loading of PPy on Co-Co@Ni-Fe PBA-coated CP substrate and bare CP substrate were 0.42 and 0.29 mg cm^{-2}, respectively.

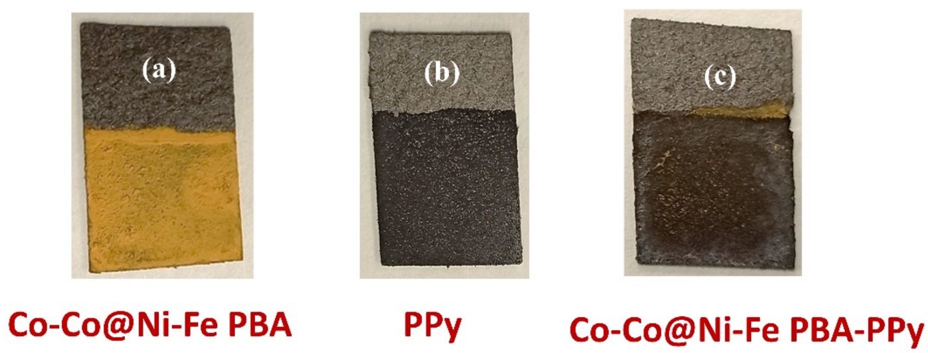

Fig S2. Photographic images (a) Co-Co@Ni-Fe core-shell PBA; (b) PPy; (c) Co-Co@Ni-Fe PBA-PPy composite deposited on CP substrates.

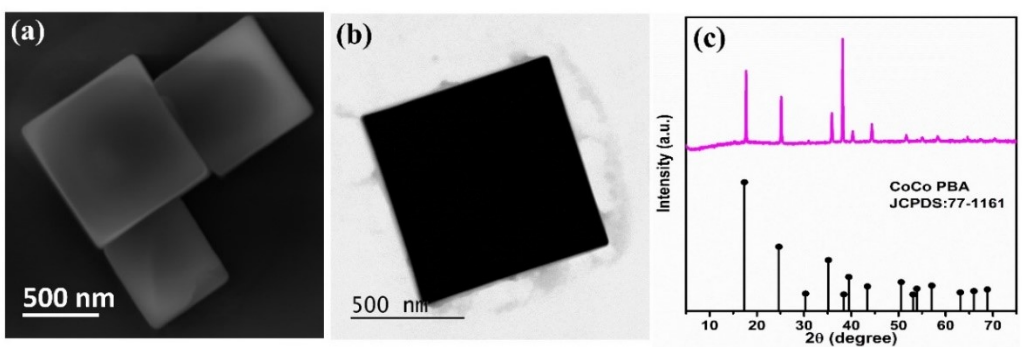

Fig S3. (a) SEM; (b) TEM image; (c) XRD of Co-Co PBA nanocubes.

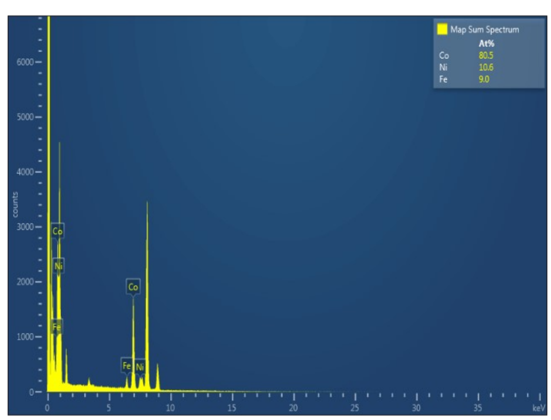

Fig S4. EDX spectrum of Co-Co@Ni-Fe core-shell PBA nanocubes.

Table S1. Summary of the ICP-OES analysis

Composition (at %)				
Sample	**Co**	**Fe**	**Ni**	**Ni/Fe**
Co-Co PBA	100	-	-	-
Co-Co@Ni-Fe PBA	43.78	22.31	33.91	1.52

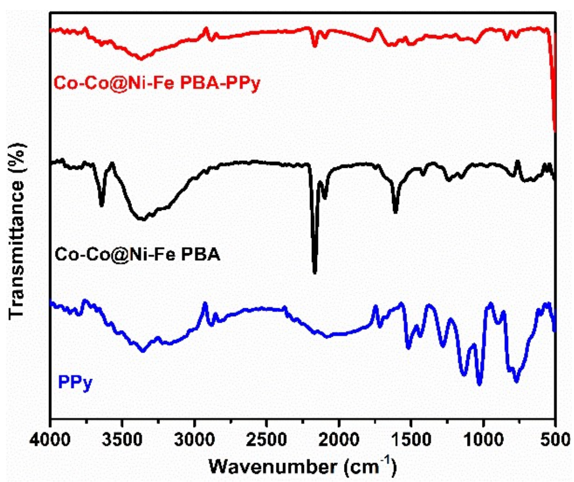

Fig S5. FTIR spectra of PPy, Co-Co@Ni-Fe PBA, and Co-Co@Ni-Fe PBA-PPy composite deposited on FTO substrates.

Fig S5 shows the FTIR spectra of PPy, Co-Co@Ni-Fe PBA, and Co-Co@Ni-Fe PBA-PPy composite deposited on FTO substrates. The FTIR spectrum of the PPy electrode showed peaks at 1,276 and 1,024 cm^{-1}, associated with the C–N stretching and C–H deformation vibrations, respectively.[1] The peaks at 1,440 cm^{-1} corresponded to the C–N stretching vibrations in the pyrrole ring, while the peak around 1,140 cm^{-1} was related to the doping state of PPy.[1] The small peaks at 3,450 cm^{-1} were assigned to the N–H stretching in PPy.[2] The peaks at 900 and 818 cm^{-1} were attributed to C–H wagging.[3] For Co-Co@Ni-Fe PBA, the peak at 3,390 and 1,610 cm^{-1} were assigned to characteristic O-H stretching vibration and H–O–

H bending vibration, demonstrating the presence of H_2O molecules.[4] The dominant peaks at ~2,158 cm^{-1} and ~2,113 cm^{-1} corresponded to the CN^- group.[4,5] The spectrum of Co-Co@Ni-Fe PBA-PPy composite showed peaks of both PPy and PBA, thus confirming the fabrication of PPy-enrobed PBA electrodes.

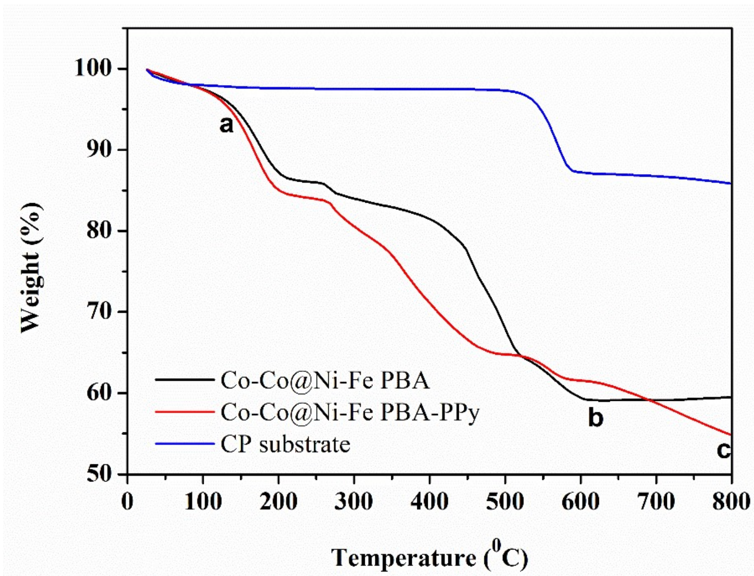

Fig S6. Thermal gravimetric analysis (TGA) plot for Co-Co@Ni-Fe PBA and Co-Co@Ni-Fe PBA-PPy composite deposited on CP substrate.

TGA curves Co-Co@Ni-Fe PBA and Co-Co@Ni-Fe PBA-PPy underwent a weight loss of 3.4% from room temperature to 140°C, displaying moisture evaporation. For Co-Co@Ni-Fe PBA, the three mass losses of 37.3% between 140 to 600^{0}C (from point a to b) corresponded to the complete decomposition of the cyanide bridges followed by stabilizing up to 800^{0}C [6–8]; this mass loss pattern well resembled the NiCo-PBA [9]. Furthermore, the Co-Co@Ni-Fe PBA-PPy composite showed mass loss up to 800^{0}C (from point a to c), which is the combined decomposition of the Co-Co@Ni-Fe PBA along with the polypyrrole network. This TGA investigation revealed that 45.24% of the total mass of Co-Co@Ni-Fe PBA-PPy is lost, whereas to Co-Co@Ni-Fe PBA lost 40.65% of the total mass, indicating 4.59% extra mass loss of Co-Co@Ni-Fe PBA-PPy is due to PPy decomposition which is around approximately 0.4 mg cm^{-2}. This result was well-coincided with the estimation of the PPy loading mass ad discussed in Section 2.4.

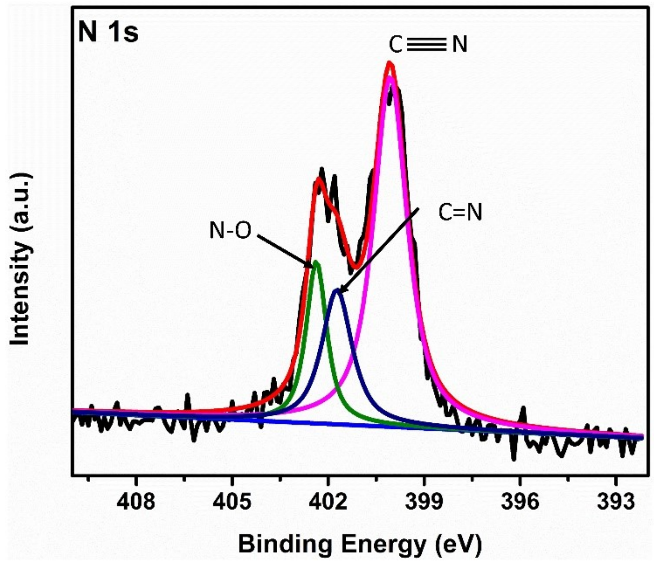

Fig S7. High-resolution XPS spectrum of N 1s for Co-Co@Ni-Fe PBA-PPy composite.

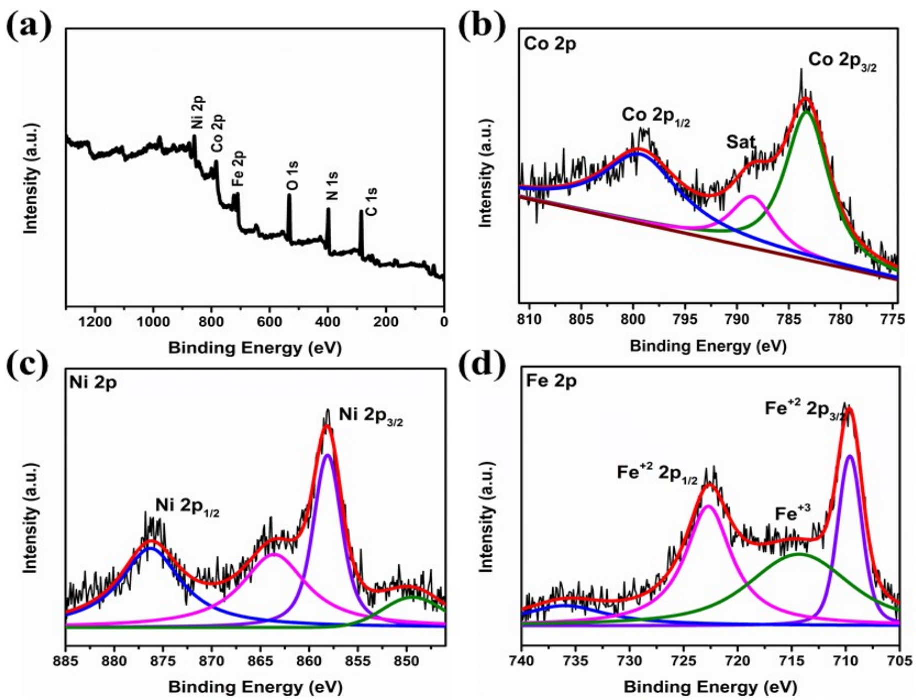

Fig S8. (a) XPS survey spectrum of Co-Co@Ni-Fe core-shell PBA; high-resolution XPS spectra of (b) Co 2p; (c) Ni 2p; (d) Fe 2p.

The peaks centered at 783.4 eV and 798.9 eV corresponded to the Co $2p_{3/2}$ and $2p_{1/2}$ signals of Co^{+2} (**Fig S8b**) [10,11]. The energy difference of 15.5 eV between Co $2p_{3/2}$ and $2p_{1/2}$ splitting was characteristic of the Co_3O_4 [12,13]. The presence of a satellite peak at a binding energy of 788.4 eV further demonstrated the existence of cobalt oxides [14,15]. This peak shifted to higher binding energy in the composite. In the high-resolution Ni 2p spectrum, the spin-orbital doublet peaks at 875.6 eV and 857.9 eV corresponded to the Ni $2p_{1/2}$ and Ni $2p_{3/2}$ of Ni^{2+} (**Fig S8c**) [16]. The peak at 863.5 eV was the satellite peak of Ni^{+2} [17]. The XPS peaks presented in **Fig S8d** at 709.7 eV and 722.6 eV represented the binding energy of Fe $2p_{3/2}$ and Fe $2p_{1/2}$ of Fe^{2+}, respectively [18]. The peak at 714.3 indicated the presence of Fe^{3+} [19]. The XPS study further confirmed the presence of Fe^{2+}/Fe^{3+} redox couple in the core-shell PBA.

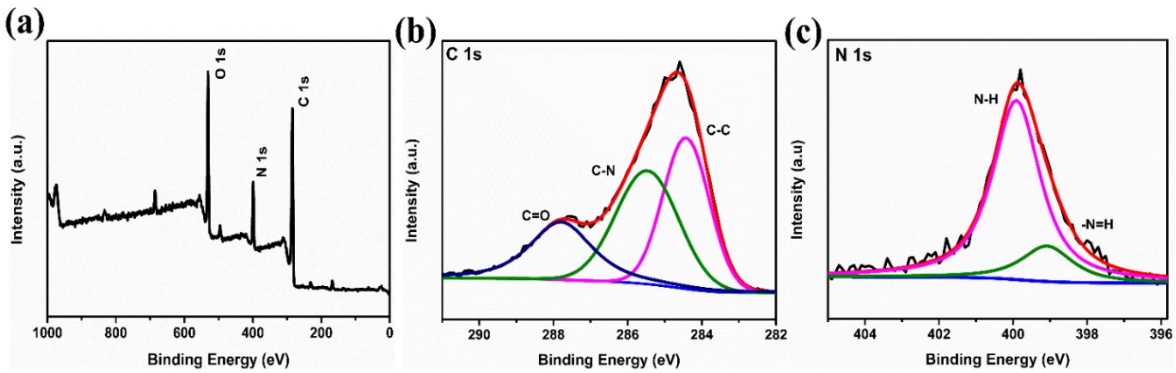

Fig S9. (a) XPS survey spectrum of PPy; high-resolution XPS spectra of (b) C 1s; (c) N 1s.

The detailed chemical state of PPy was characterized by the deconvolution of the C1s and N1s spectra (**Fig S9b-c**). The C1s spectrum of PPy could be fitted into C−C at 284.5 eV, C−N at 285.3 eV, and C=O at 287.9 eV (**Fig S9b**) [20,21]. The termination reaction and/or subsequent reaction during electro-polymerization may have produced the C=O group. For N 1s, the neutral amine nitrogen (N-H) was allocated to the significant peak component at 399.5 eV, while the low-intensity peak at 397.6 eV was assigned to imine nitrogen (N=), (**Fig S9c**) [22].

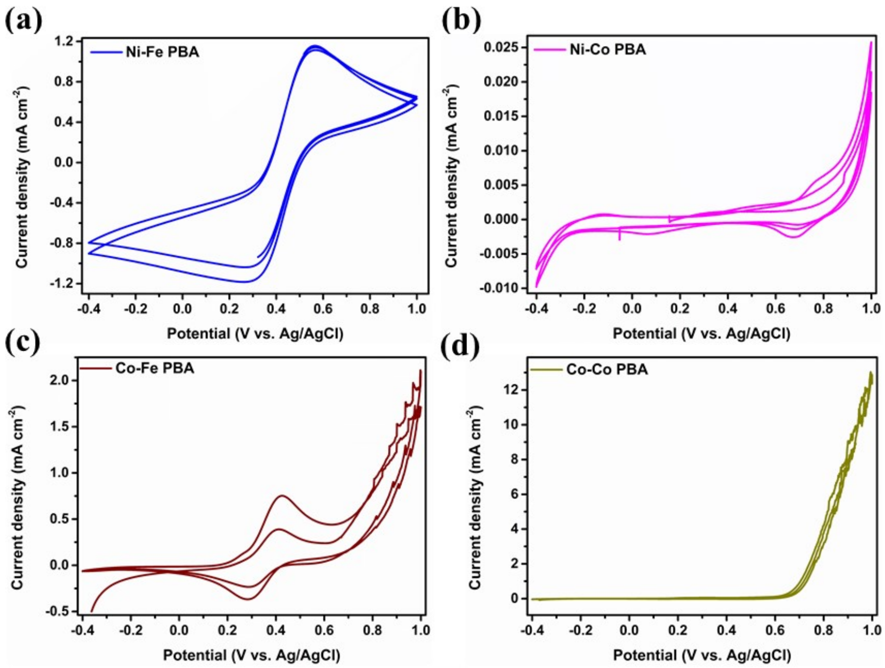

Fig S10. CVs of (a) Ni-Fe PBA; (b) Ni-Co PBA; (c) Co-Fe PBA; (d) Co-Co PBA that were deposited on glassy carbon electrode and submerged in 1.0 M Na_2SO_4.

To examine the electrochemical redox behaviors of different metals composing the PBA, we synthesized bimetallic PBA nanocubes with various metal combinations. The CV measurements of Ni-Fe PBA (**Fig S10a**) showed a well-distinguished single pair of redox peaks between 0.3 to 0.5 V; which was attributed to the $Fe^{II/III}$ couple because no prominent peaks were seen for Ni-Co PBA (**Fig S10b**) and Co-Co PBA (**Fig S10d**) combinations. Co-Co PBA showed the water oxidation wave (**Fig S10d**). Likewise, Co-Fe PBA (**Fig S10c**) developed a pair of redox peaks in the same potential range (0.3 to 0.5 V) displayed by Ni-Fe PBA (**Fig S10a**), followed by an increase in current. Ni-Fe PBA and Co-Fe PBA, where Fe^{II} was present, showed redox peaks in the same potential range; hence we assigned this electrochemical behavior to the $Fe^{II/III}$ redox couple. The CVs of Ni-Fe PBA showed well-developed redox peaks with a higher integral area than the Co-Fe PBA. Therefore, we used homogeneous Ni-Fe PBA shell coating over the Co-Co PBA core template to synthesize the Co-Co@Ni-Fe PBA redox probe. Here, the Co-Co PBA core provided excellent electrical conductivity.

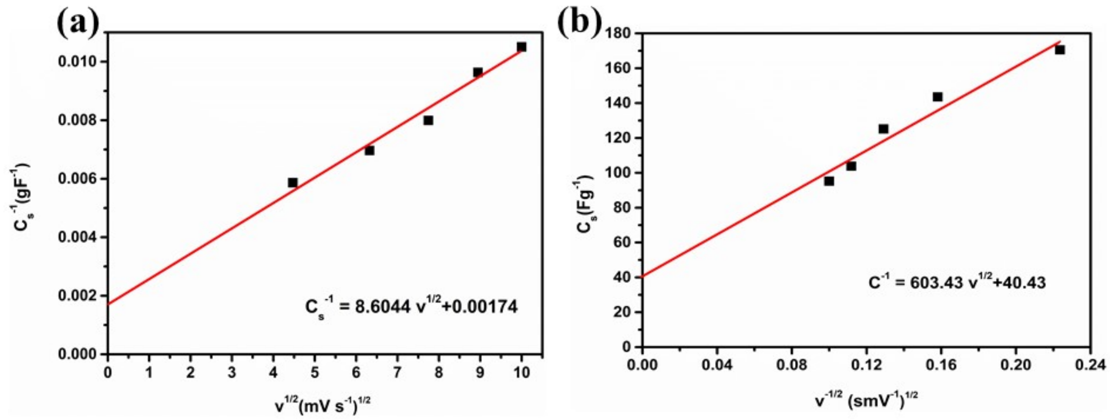

Fig S11. (a) A plot of the reciprocal of specific capacitance (C_s^{-1}) vs. the square root of scan rate; (b) the plot of the specific capacitance vs. the reciprocal of the square root of scan rate.

Trasatti method wa used to estimate the contribution of capacitive and diffusive currents to the total capacitance value by using a reported protocol [23–26].

Step 1: The following equation determines the average specific capacitance (C_s, F g^{-1}) values from CVs at different scan rates (**Eq. S1**).

$$C_s = \frac{1}{m\upsilon\Delta V}\int i\,(V)dV \qquad \textbf{Eq. S1}$$

Here, *m* signifies the mass of electrode materials, υ is the scan rate, *i* denotes the current (A), and ΔV is a potential window (V). The area under the CV curve represents the current integration.

Step 2: A linear correlation between the reciprocal of the specific capacitance and the square root of scan rates should be observed for the semi-infinite diffusion of ions to the electrode/electrolyte interface from the bulk electrolyte (**Eq. S7**).

$$C_s^{-1} = constant.\,\upsilon^{1/2} + C_T^{-1} \qquad \textbf{Eq. S7}$$

C_s is the calculated specific capacitance, υ is the scan rate, and C_T denotes the maximum total capacitance. The maximum total capacitance (C_T) will be the sum of diffusion-controlled inner capacitance (C_i) and non-diffusion-controlled outer-surface capacitance (C_o). C_T equals the reciprocal y-intercept of the C_s^{-1} vs. $\upsilon^{1/2}$ (**Fig S11a**).

Step 3: By assuming semi-infinite ions diffusion pattern, the calculated specific capacitances (C_s) vary linearly with the reciprocal of the square root of scan rates ($\upsilon^{-1/2}$) as described by equation (**Eq. S8**).

$$C_S = constant.\upsilon^{-1/2} + C_o \qquad \textbf{Eq. S8}$$

C_s is the calculated specific capacitance, and υ is the scan rate. C_o equals the y-intercept of the C_s vs. $\upsilon^{-1/2}$ plot (**Fig S11b**). The subtraction of C_o from C_T can determine the diffusion-controlled inner capacitance (C_i)

Step 4: The percentage of capacitance contribution can be determined by the following equations.

$$C_o\% = \frac{C_o}{C_T} \times 100\% \qquad \textbf{Eq. S9}$$

$$C_i\% = \frac{C_i}{C_T} \times 100\% \qquad \textbf{Eq. S10}$$

Trasatti method quantifies the diffusion-controlled and non-diffusion-controlled contribution to total capacitance, supporting the diffusion-controlled contribution as the dominant charge-storage mechanism. Over 92.91% of the specific capacitance came from the diffusive contribution of the Co-Co@Ni-Fe core-shell PBA, which was delivered by the $Fe^{II/III}$ redox couples.

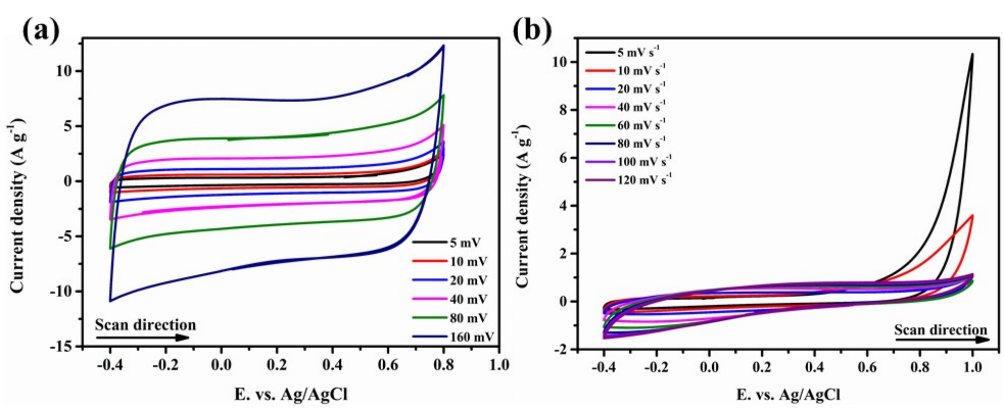

Fig S12. The CVs of PPy (deposited on CP) performed up to (a) 0.8 V; (b) 1.0 V vs Ag/AgCl in 1.0 M Na_2SO_4 at different scan rates

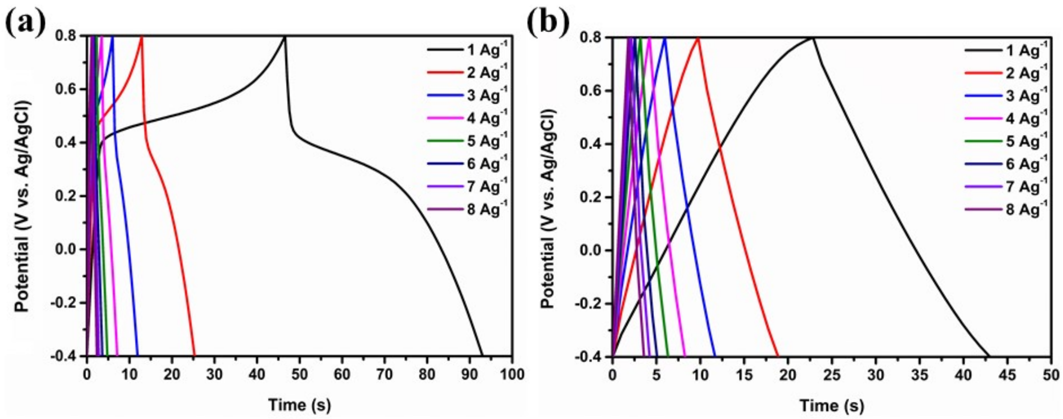

Fig S13. The GCD curves of (a) PBA; (b) PPy in 1.0 M Na_2SO_4 at different current densities.

Table S2. Comparison of PBA and its derivative composites for supercapacitor electrodes.

Compounds	Electrolyte	Efficiency	Cyclic retention	Ref.
Manganese hexacyanoferrate/graphene oxide nanocomposite	1.0 M Na_2SO_4	215.2 F g^{-1} at 1A g^{-1}	66.8% retention at 0.8 A g^{-1} over 2000 cycles	27
Prussian blue/reduced graphene oxide nanocomposite	1.0 M Na_2SO_4	286 F g^{-1} at 0.3 A g^{-1}	92% retention at 2 A g^{-1} over 1000 cycles	28
Hollow-structured cobalt hexacyanoferrate	0.5 M Na_2SO_4	284 F g^{-1} at 1 A g^{-1}	92% retention at 10 A g^{-1} over 5000 cycles	29
cobalt hexacyanoferrate/reduced graphene oxide hydrogels	1.0 mol L^{-1} KNO_3	225.2 F g^{-1} at 1 A g^{-1}	82% retention at 5 A g^{-1} over 10000 cycles	30
Cobalt hexacyanoferrate submicroboxes	0.5 M Na_2SO_4	288 F g^{-1} at 0.5 A g^{-1}	93.1% retention at 10 A g^{-1} over 8000 cycles	31
Prussian-blue-doped super activated carbon	1.0 M KCl	263.7 F g^{-1} at 5 A g^{-1}	94.8% retention at 10 A g^{-1} over 1500 cycles	32
Manganous hexacyanoferrate	0.5 M Na_2SO_4	238 F g^{-1} at 1 mA cm^{-2}	87% retention at 1 mA cm^{-2} over 1000 cycles	33
Meso Ni-hexacyanoferrate	1.0 M Na_2SO_4	184 F g^{-1} at 5 mV s^{-1}	-	34
Meso Cu-hexacyanoferrate	1.0 M Na_2SO_4	243 F g^{-1} at 5 mV s^{-1}	-	34
Meso Co-hexacyanoferrate	1.0 M Na_2SO_4	295 F g^{-1} at 5	-	34

		mV s^{-1}		
N-doped carbon nanowires supported Fe2O3 nanocubes	5.0 M Na_2SO_4	268.6 F g^{-1} at 10 mV s^{-1}	-	[35]
NiO/Fe_3O_4	6.0 M KOH	228 F g^{-1} at 1 A g^{-1}	75% retention at 5 A g^{-1} over 3000 cycles	[36]
Co_3O_4/Fe_3O_4	6.0 M KOH	143 F g^{-1} at 1 A g^{-1}	79% retention at 5 A g^{-1} over 3000 cycles	[36]
NiO/Co_3O_4/Fe_3O_4	6.0 M KOH	529 F g^{-1} at 1 A g^{-1}	86% retention at 5 A g^{-1} over 3000 cycles	[36]
Co-Co@Ni-Fe PBA-PPy composite	**1.0 M Na_2SO_4**	**265 F g^{-1} (318 C g^{-1}) at 1A g^{-1}**	**90% retention at 15 A g^{-1} over 2000 cycles**	**This Work**

Table S3. The fitting results of the impedance electrochemical element parameters of various samples.

Electrocatalysts	R_s	Q	R_{ct}	W
PBA-PPy	3.482	0.261	20.23	0.018
PBA	2.742	0.686	34.65	0.046

$\mathbf{R_s}$ is the uncompensated solution resistance in the equivalent circuit; **Q** is the constant phase element (CPE) related to the electrochemical double-layer capacitance at the catalyst|electrolyte interface; $\mathbf{R_{ct}}$ is the charge transfer resistance between the interfaces; **W** is Warburg diffusion resistance.

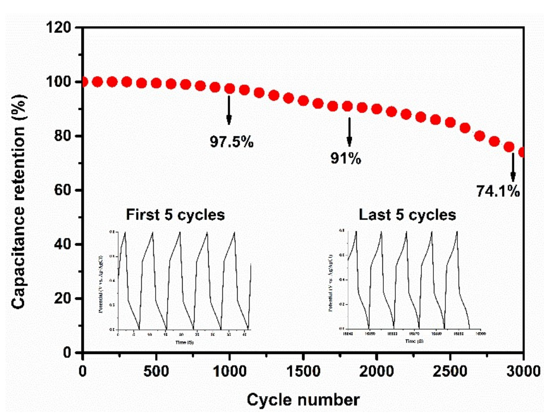

Fig S14. Cyclic stability of Co-Co@Ni-Fe PBA-PPy composite at 15 Ag^{-1} for 3,000 cycles in 1.0 M Na_2SO_4.

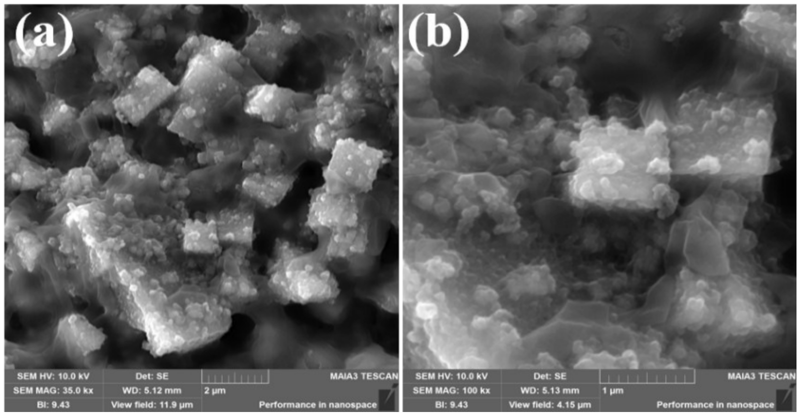

Fig S15. HR-SEM images of Co-Co@Ni-Fe PBA-PPy composite after 3000 cycles of cyclic stability.

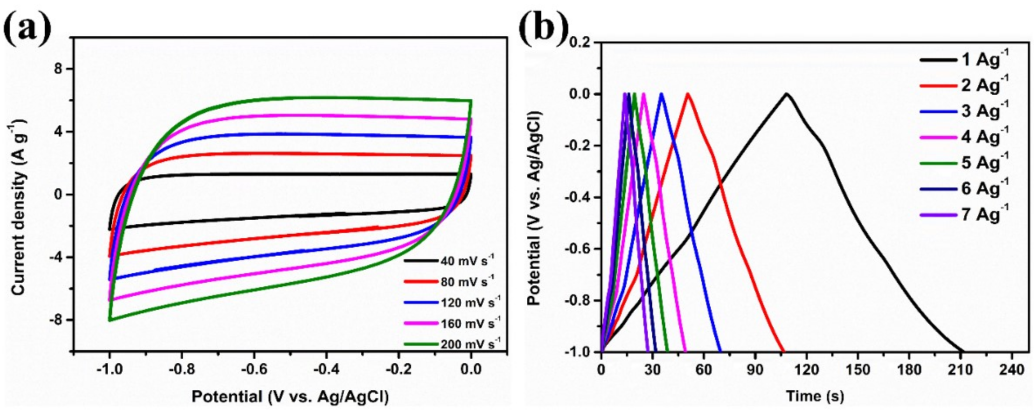

Fig S16. CVs (a) and GCD curves (b) of AC in 1.0 M Na_2SO_4 at three-electrode configuration

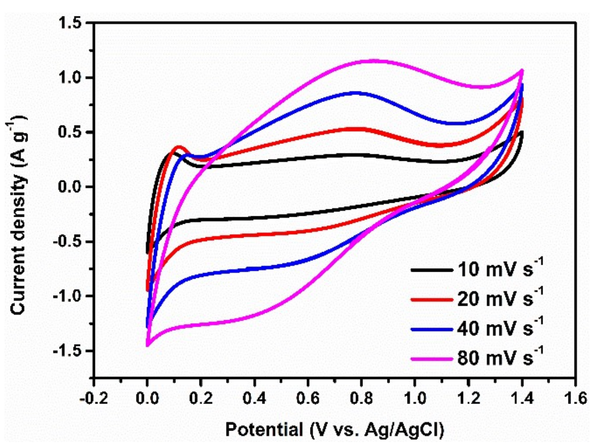

Fig S17. CVs of symmetric supercapacitor cell configuration constructed by taking an equal amount of Co-Co@Ni-Fe PBA-PPy as positive and negative electrodes. Both positive and negative electrodes were placed one upon another using filter paper soaked in 1 M Na_2SO_4 as the separator.

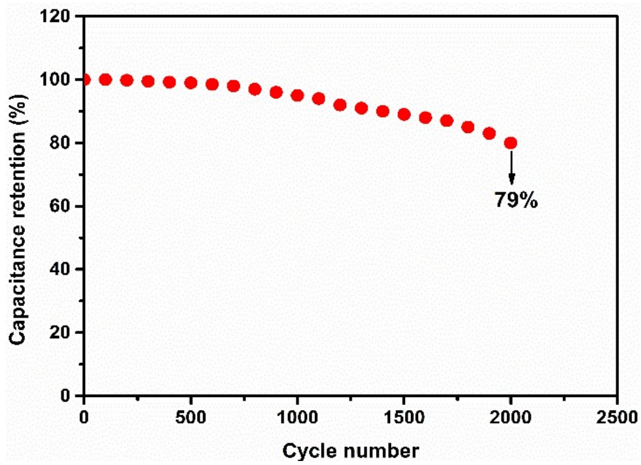

Fig S18. The cyclic stability of the as-fabricated Co-Co@Ni-Fe PBA-PPy//AC device.

Table S4. Comparison of PBA and its derivative composites used in ASC devices.

ASC based electrode	Operating potential window (V)	Specific capacitance (Fg^{-1})	Energy density (Wh kg^{-1})	Power density (W kg^{-1})	Cyclic retention	Ref.
P(Ni, Co, Fe)//AC	1.6	42.1 F g^{-1} at 0.1 A g^{-1}	15	4000	93.3% retention at 5 A g^{-1} over 5000 cycles	[37]
CeO_2@NiFe-LDH//AC	1.6	67.3 F g^{-1} at 0.1 A g^{-1}	21.2	7500	77.7% retention at 10 A g^{-1} over 5000 cycles	[38]
Graphene@prussian blue//AC	1.8	44.61 F g^{-1} at 0.5 A g^{-1}	20.1	2700	87.5% retention at 5 A g^{-1} over 5000 cycles	[39]
Cobalt hexacyanoferrate//AC	1.4	65.5 F g^{-1} at 0.5 A g^{-1}	17.4	1196	91% retention at 1 A g^{-1} over 6000 cycles	[40]
Co-Co@Ni-Fe PBA-PPy//AC	**1.6**	**64 F g^{-1} (90 C g^{-1}) at 1 A g^{-1}**	**20**	**1996**	**79% retention at 10 A g^{-1} over 2000 cycles**	**This work**

REFERENCES

1 F. Wu, A. Xie, M. Sun, Y. Wang and M. Wang, Reduced graphene oxide (RGO) modified spongelike polypyrrole (PPy) aerogel for excellent electromagnetic absorption, *J. Mater. Chem. A*, 2015, **3**, 14358–14369.

2 B. S. Singu and K. R. Yoon, Mesoporous polypyrrole-Ag nanocomposites for supercapacitors, *J. Alloys Compd.*, 2018, **742**, 610–618.

3 M. A. Chougule, S. G. Pawar, P. R. Godse, R. N. Mulik, S. Sen and V. B. Patil, Synthesis and Characterization of Polypyrrole (PPy) Thin Films, *Soft Nanosci. Lett.*, 2011, **01**, 6–10.

4 T. Wang, Q. Pang, B. Li, Y. Chen and J. Z. Zhang, Three-dimensional core–shell CoFe Prussian blue analog at NiCoFe layered ternary hydroxide electrocatalyst for efficient oxygen evolution reaction, *Appl. Phys. Lett.*, 2021, **118**, 233903.

5 C. Xuan, K. Xia, W. Lei, W. Xia, W. Xiao, L. Chen, H. L. Xin and D. Wang, Composition-dependent electrocatalytic activities of NiFe-based selenides for the oxygen evolution reaction, *Electrochim. Acta*, 2018, **291**, 64–72.

6 M. Vondrova, T. M. McQueen, C. M. Burgess, D. M. Ho and A. B. Bocarsly, Autoreduction of Pd−Co and Pt−Co Cyanogels: Exploration of Cyanometalate Coordination Chemistry at Elevated Temperatures, *J. Am. Chem. Soc.*, 2008, **130**, 5563–5572.

7 J. Huang, Q. Shan, Y. Fang, N. Zhao and X. Feng, Shape-controlled Mn–Fe PBA derived micromotors for organic pollutant removal, *New J. Chem.*, 2022, **46**, 8611–8618.

8 V. Trannoy, A. Bordage, J. Dezalay, R. Saint-Martin, E. Rivière, P. Beaunier, C. Baumier, C. La Fontaine, G. Fornasieri and A. Bleuzen, Towards the synthesis of mixed oxides with controlled stoichiometry from Prussian blue analogues, *CrystEngComm*, 2019, **21**, 3634–3643.

9 H. Zhang, Q. Jiang, J. H. L. Hadden, F. Xie and D. J. Riley, Pd Ion-Exchange and Ammonia Etching of a Prussian Blue Analogue to Produce a High-Performance Water-Splitting Catalyst, *Adv. Funct. Mater.*, 2021, **31**, 2008989.

10 H.-M. Zhang and C. Zhu, Co nanoparticles-embedded N, S-codoped hierarchically porous graphene sheets as efficient bifunctional electrocatalysts for oxygen reduction reaction and hydrogen evolution reaction, *J. Mater. Res. Technol.*, 2020, **9**, 16270–16279.

11 R. Muruganantham, J.-S. Lu and W.-R. Liu, Spinel rGO Wrapped CoV2O4 Nanocomposite as a

Novel Anode Material for Sodium-Ion Batteries, *Polymers (Basel).*, 2020, **12**, 555.

12 P. W. Menezes, A. Indra, A. Bergmann, P. Chernev, C. Walter, H. Dau, P. Strasser and M. Driess, Uncovering the prominent role of metal ions in octahedral versus tetrahedral sites of cobalt–zinc oxide catalysts for efficient oxidation of water, *J. Mater. Chem. A*, 2016, **4**, 10014–10022.

13 A. Indra, P. W. Menezes, C. Das, C. Göbel, M. Tallarida, D. Schmeiβer and M. Driess, A facile corrosion approach to the synthesis of highly active CoO x water oxidation catalysts, *J. Mater. Chem. A*, 2017, **5**, 5171–5177.

14 Y. Zhang, L. Liu, Q. Deng, W. Wu, Y. Li, X. Ren, P. Zhang and L. Sun, Hybrid CuO-Co3O4 nanosphere/RGO sandwiched composites as anode materials for lithium-ion batteries, *Chinese J. Chem. Eng.*, 2022, **47**, 185–192.

15 H. Kierzkowska-Pawlak, E. Kruszczak and J. Tyczkowski, Catalytic activity of plasma-deposited Co3O4-based thin films for CO2 hydration – A new approach to carbon capture applications, *Appl. Catal. B Environ.*, 2022, **304**, 120961.

16 Y. Lan, H. Xing, Y. Zong, Y. Sun, L. Zhang, Y. Wang, X. Li and X. Zheng, Hierarchical Ni2P@Ni(OH)2 architectures supported on carbon cloth as battery-type electrodes for hybrid supercapacitors with boosting specific capacitance and cycle stability, *J. Mater. Sci. Mater. Electron.*, 2021, **32**, 7973–7986.

17 B. Malik, S. Majumder, R. Lorenzi, I. Perelshtein, M. Ejgenberg, A. Paleari and G. D. Nessim, Promising Electrocatalytic Water and Methanol Oxidation Reaction Activity by Nickel Doped Hematite/Surface Oxidized Carbon Nanotubes Composite Structures, *Chempluschem*, , DOI:10.1002/cplu.202200036.

18 Y. Zeng, X. Zhang, X. Mao, P. K. Shen and D. R. MacFarlane, High-capacity and high-rate Ni-Fe batteries based on mesostructured quaternary carbon/Fe/FeO/Fe3O4 hybrid material, *iScience*, 2021, **24**, 102547.

19 Y. Xie, Z. Zhou, N. Yang and G. Zhao, An Overall Reaction Integrated with Highly Selective Oxidation of 5-Hydroxymethylfurfural and Efficient Hydrogen Evolution, *Adv. Funct. Mater.*, 2021, **31**, 2102886.

20 S. K. Das, C. Dickinson, F. Lafir, D. F. Brougham and E. Marsili, Synthesis, characterization and catalytic activity of gold nanoparticles biosynthesized with Rhizopus oryzae protein extract, *Green Chem.*, 2012, **14**, 1322.

21 M. Šetka, R. Calavia, L. Vojkůvka, E. Llobet, J. Drbohlavová and S. Vallejos, Raman and XPS studies of ammonia sensitive polypyrrole nanorods and nanoparticles, *Sci. Rep.*, 2019, **9**, 8465.

22 J. Cao, Y. Wang, J. Chen, X. Li, F. C. Walsh, J.-H. Ouyang, D. Jia and Y. Zhou, Three-dimensional graphene oxide/polypyrrole composite electrodes fabricated by one-step electrodeposition for high performance supercapacitors, *J. Mater. Chem. A*, 2015, **3**, 14445–14457.

23 S. Fleischmann, J. B. Mitchell, R. Wang, C. Zhan, D. Jiang, V. Presser and V. Augustyn, Pseudocapacitance: From Fundamental Understanding to High Power Energy Storage Materials, *Chem. Rev.*, 2020, **120**, 6738–6782.

24 S. Ardizzone, G. Fregonara and S. Trasatti, “Inner” and “outer” active surface of RuO2 electrodes, *Electrochim. Acta*, 1990, **35**, 263–267.

25 H. Vogt, Note on a method to interrelate inner and outer electrode areas, *Electrochim. Acta*, 1994, **39**, 1981–1983.

26 A. Cymann-Sachajdak, M. Graczyk-Zajac, G. Trykowski and M. Wilamowska-Zawłocka, Understanding the capacitance of thin composite films based on conducting polymer and carbon nanostructures in aqueous electrolytes, *Electrochim. Acta*, 2021, **383**, 138356.

27 T. Yang, J. Gao, L. Zhou, Q. He, S. Chen, P. He, B. Jia, H. Lei, F. Dong and H. Zhang, Tailored manganese hexacyanoferrate/graphene oxide nanocomposites: one-pot facile synthesis and favorable capacitance behavior for supercapacitors, *J. Mater. Sci. Mater. Electron.*, 2020, **31**, 2720–2728.

28 J.-G. Wang, L. Ren, Z. Hou and M. Shao, Flexible reduced graphene oxide/prussian blue films for hybrid supercapacitors, *Chem. Eng. J.*, 2020, **397**, 125521.

29 X. Yin, H. Li, H. Wang, Z. Zhang, R. Yuan, J. Lu, Q. Song, J.-G. Wang, L. Zhang and Q. Fu, Self-Templating Synthesis of Cobalt Hexacyanoferrate Hollow Structures with Superior Performance for Na-Ion Hybrid Supercapacitors, *ACS Appl. Mater. Interfaces*, 2018, **10**, 29496–29504.

30 X. Zhang, J. Jiang, Y. Chen, K. Cheng, F. Yang, J. Yan, K. Zhu, K. Ye, G. Wang, L. Zhou and D. Cao, A flexible and high voltage symmetric supercapacitor based on hybrid configuration of cobalt hexacyanoferrate/reduced graphene oxide hydrogels, *Chem. Eng. J.*, 2018, **335**, 321–329.

31 J.-G. Wang, Z. Zhang, X. Zhang, X. Yin, X. Li, X. Liu, F. Kang and B. Wei, Cation exchange formation of prussian blue analogue submicroboxes for high-performance Na-ion hybrid supercapacitors, *Nano Energy*, 2017, **39**, 647–653.

32 Q. Wang, Prussian-Blue-Doped Super-Activated Carbon as a High Performance Supercapacitor Electrode Material, *Int. J. Electrochem. Sci.*, 2016, **11**, 5679–5690.

33 K. Lu, D. Li, X. Gao, H. Dai, N. Wang and H. Ma, An advanced aqueous sodium-ion supercapacitor with a manganous hexacyanoferrate cathode and a Fe 3 O 4 /rGO anode, *J. Mater. Chem. A*, 2015, **3**, 16013–16019.

34 Y. Yue, Z. Zhang, A. J. Binder, J. Chen, X. Jin, S. H. Overbury and S. Dai, Hierarchically Superstructured Prussian Blue Analogues: Spontaneous Assembly Synthesis and Applications as Pseudocapacitive Materials, *ChemSusChem*, 2015, **8**, 177–183.

35 Y. Zhang, R. Lin, Y. Fu, X. Wang, X. Yu, J. Li, Y. Zhu, S. Tan and Z. Wang, Metal-organic framework derived Fe2O3 nanocubes on intertwined N-doped carbon nanowires for fiber-shaped supercapacitor, *Mater. Lett.*, 2018, **228**, 9–12.

36 F. Song, G. Zan, Y. Chen, Q. Wu and Y. Xu, In situ transformation of iron-group ternary metal oxides nanocubes from Co/Ni-PBA for high-performance supercapacitors, *J. Alloys Compd.*, 2018, **741**, 633–641.

37 X. Zhang, M. I. Alvarado-Ávila, Y. Liu, D. Yu, F. Ye and J. Dutta, Self-sacrificial growth of hierarchical P(Ni, Co, Fe) for enhanced asymmetric supercapacitors and oxygen evolution reactions, *Electrochim. Acta*, 2023, **438**, 141582.

38 T. Zhou, W. Zhang, H. Fu, J. Fang, C. Chen and Z. Wang, Preparation of 3D CeO2@NiFe-LDH composites derived from prussian blue analogues for high performance supercapacitors, *Mater. Sci. Semicond. Process.*, 2022, **150**, 106913.

39 S.-C. Wang, M. Gu, L. Pan, J. Xu, L. Han and F.-Y. Yi, The interlocked in situ fabrication of graphene@prussian blue nanocomposite as high-performance supercapacitor, *Dalt. Trans.*, 2018, **47**, 13126–13134.

40 Z. Song, W. Liu, Q. Yuan, Q. Zhou, G. Liu and Z. Zhao, Microporous/mesoporous cobalt hexacyanoferrate nanocubes for long-cycle life asymmetric supercapacitors, *J. Mater. Sci. Mater. Electron.*, 2018, **29**, 14897–14905.